

1 **Regenerable Magnetic Iron Oxide Incorporated Chitosan Beads for Sulfate**
2 **(SO₄²⁻) Removal from Wastewater: Isotherms, Kinetics and Mechanism**

3 Uswa Zahra¹, Imran Ahmad Khan¹, Asad Ullah Khan¹, Muhammad Yasir^{2,*}, Wenjuan Zhang³,
4 Kashif Mairaj Deen⁴, Edouard Asselin⁴, Rehan Sadiq⁵, Muhammad Nouman Aslam Khan¹, Nasir
5 M. Ahmad^{1,*}

6 ¹ *Polymer Research Lab, School of Chemical and Materials Engineering (SCME), National*
7 *University of Sciences and Technology (NUST), H-12, Islamabad, Pakistan*

8 ² *Centre of Polymer Systems, University Institute, Tomas Bata University in Zlín, Třída Tomáše*
9 *Bati 5678, 76001 Zlín, Czech Republic*

10 ³ *State Key Laboratory of Advanced Metallurgy, University of Science and Technology Beijing,*
11 *Beijing 100083, China*

12 ⁴ *Department of Materials Engineering, The University of British Columbia, Vancouver, V6T*
13 *1Z4, BC, Canada*

14 ⁵ *Department of Civil Engineering, School of Engineering, The University of British Columbia*
15 *Okanagan Campus, EME4242 - 1137 Alumni Ave, Kelowna, BC, Canada*

16 ***Corresponding authors:** M. Yasir (yasir@utb.cz), N. M. Ahmad
17 (nasir.ahmad@scme.nust.edu.pk)

18 **Abstract**

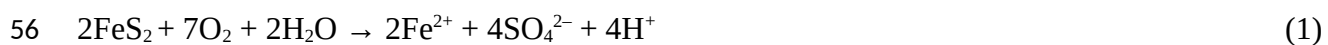
19 Sulfate contamination removal from mine waste and industrial water is a primary environmental
20 concern, with high concentrations leading to diseases such as anorexia, diarrhea, dehydration,
21 and gastrointestinal dysfunction. This research focuses on the preparation of iron oxide-
22 incorporated chitosan beads (IOICBs) for the effective adsorption removal of sulfate. The
23 IOICBs were synthesized by a chemical co-precipitation approach rigorously characterized by
24 Scanning Electron Microscopy, X-ray Diffraction, Brunauer-Emmett-Teller analysis, Fourier
25 Transform Infrared Spectroscopy, and energy-dispersive X-ray mapping for structural, chemical,
26 and morphological properties. The sulfate adsorption on IOICBs was investigated in batch mode
27 studies using UV-Vis spectroscopy. The effect of several parameters, such as adsorbent dosage,

28 pH, initial concentration, and contact time, on the sorption capacity of the IOICBs was studied.
29 The IOICBs have a high efficacy for sulfate removal from contaminated water at pH 2 with a
30 maximum sorption capacity of 147.7 mg/g at room temperature. The mechanism suggested that
31 the presence of acidic NH_4^+ functional groups on the surface of chitosan facilitates the
32 chemisorption of the sulfate ions. The adsorption equilibrium is in good agreement with the
33 Langmuir Isotherm ($R^2 = 0.997$), and the kinetics analysis suggests the adsorption is a pseudo-
34 second-order process ($R^2 = 0.992$), confirming the chemisorption of sulfate species on IOICBs.
35 After sulfate adsorption, the IOICBs were regenerated in 0.1 M NaOH solution and reused for
36 multiple sorption/desorption cycles, and the reusability remained at over 83% after four
37 consecutive cycles. Thus, IOICBs are potential absorbents for removing industrial pollutants
38 such as sulfate ions from wastewater.

39 **Keywords:** Adsorption, Chitosan bead, Iron oxide, Sulfate removal, Wastewater treatment

40 1. INTRODUCTION

41 During mining and hydrometallurgical processing of sulfide minerals, i.e., pyrite, the oxidation
42 of sulfide sulfur results in the generation of a high amount of sulfate in the processed water
43 (reaction 1). For instance, neutral or acid mine drainage and effluent water released from the
44 upstream and downstream metal extraction processes are significant sources of acidity and
45 sulfates in surface and groundwater. The high concentration of sulfates in natural water streams
46 could adversely affect human and aquatic life ¹⁻⁴. The maximum tolerable sulfate level in
47 industrial wastewater ranges between 250 and 500 mg/L. Typical sulfate levels in domestic
48 sewage can vary between 20 and 500 mg/L, whereas mines and industrial effluents may contain
49 several thousand mg/L of sulfate species ⁵. A modest amount of sulfate in water has a negligible
50 impact on human health. Still, when the sulfate content surpasses 500 mg/L, it can lead to acute
51 diseases such as anorexia, diarrhea, dehydration, and gastrointestinal dysfunction, whereas
52 polioencephalomalacia occurs in animals. In addition, sulfate-containing sediments in lakes,
53 rivers, and the ocean can induce detrimental impacts on the structural integrity of metallic
54 structures, i.e., pipes, ships, offshore oil and gas drilling rigs, and bridges, due to extensive
55 scaling and accelerated corrosion ^{6,7}.



57 Enriched sulfate water has been treated using a variety of techniques, including membrane
58 technologies ⁶, ion exchange ⁷, adsorption ⁸, and chemical and biological treatment methods ^{5,9}.
59 On a commercial scale, the selection of the treatment process is dependent on the mine water
60 chemistry and mining operation ¹. For instance, in the case of membrane separation processes,
61 the pre-treatment of the membrane is necessary to prevent membrane fouling. Also, membrane
62 technologies and ion exchange processes are considered uneconomical for treating large amounts
63 of contaminated mine water ^{1,5}.

64 Adsorption has proven to be one of the most cost-effective, biocompatible, and environmentally
65 friendly wastewater treatment methods ^{10,11}. For example, conventional adsorbents include
66 biomass, agricultural waste, nanosized metal oxides (NMOs), activated carbon, and others for
67 adsorption processes. Owing to the simple chemical modification process, the adsorption
68 capacity of the activated carbon, which is considered the most effective method to remove
69 contaminants from water, could be significantly enhanced. However, the retrieval of the
70 powdered activated carbon from the treated water is found to be relatively complex ¹².

71 Iron oxide has a remarkable abundance of active sites readily available for adsorption. This
72 abundance of active sites allows efficient capture of contaminants across a broad range of pH
73 values, making it suitable for a wider variety of applications than other adsorbent materials ¹³.
74 Iron oxide nanomaterials efficiently remove heavy ions; however, their frequent challenges
75 include the precipitation of Iron oxide and limited reusability ¹⁴. Polymeric-based adsorbents
76 utilizing polysaccharide chitosan as a matrix are emerging materials in adsorption science ¹⁵. Its
77 outstanding adsorption properties primarily arise from the amino ($-NH_2$) and hydroxyl ($-OH$)
78 groups present in chitosan within its polymer matrix ¹⁶. One of the critical advantages of chitosan
79 lies in its versatility of application. It can be readily adapted to various physical forms, including
80 powders ¹⁵, nanoparticles ¹⁷, hydrogels ¹⁸, fibers ¹⁹, and beads ²⁰. This makes it a highly versatile
81 material for environmental and separation processes. Recent studies have shown that chitosan
82 grafted with polyaniline and reinforced with cobalt ferrite nanoparticles forms highly efficient
83 nanocomposites for wastewater remediation, capable of removing a broad spectrum of heavy
84 metals such as Pb^{2+} , Cu^{2+} , Cd^{2+} , Zn^{2+} , and Cr^{2+} with efficiencies exceeding 95%. The optimized
85 Ch-g-PANI/CoFM-5% composite exhibited rapid adsorption equilibrium within 90 minutes,
86 followed by multilayer Freundlich isotherm behavior, and maintained strong regeneration

87 capacity over multiple cycles, underscoring its potential as a sustainable treatment material ²¹.
88 Another approach involved fabricating chitosan/gelatin membranes reinforced with graphene
89 oxide nanoplatelets grafted with natural rosin acids (GO-g-R), yielding sustainable bio-
90 membranes with enhanced strength and photocatalytic performance. The optimized CGe-GO-g-
91 R30% membrane exhibited ~ 96.5 N/mm² tensile strength, strong antibacterial activity, and up to
92 98.4% dye removal efficiency under solar irradiation, following Langmuir isotherm and pseudo-
93 second-order kinetics, while retaining reusability across cycles ²². Chitosan/polyvinyl alcohol
94 membranes incorporated with graphene oxide modified by rosin and silver nanoparticles
95 demonstrated strong dual functionality for water treatment, simultaneously targeting heavy
96 metals and microbial contaminants. The optimized composite (3 wt.% decorated GO) achieved
97 removal efficiencies between 85–99.7% for different metal ions, while also displaying notable
98 antibacterial performance and improved tensile strength (~ 48 MPa), underscoring its promise for
99 agricultural and irrigation applications ²³. Hybrid polyvinyl chloride/dapsone membranes
100 embedded with silver nanoparticles were engineered to enhance pollutant removal from
101 contaminated water, offering combined efficiency against heavy metals, microbial species, and
102 nutrient compounds such as phosphates and nitrates. The optimal composition containing 0.2%
103 Ag NPs achieved removal rates between 71–95% depending on ion type, while also improving
104 porosity, tensile strength, and antibacterial properties, making it a promising multifunctional
105 membrane for environmental and biomedical applications ²⁴. Recent work demonstrated that
106 incorporating natural Rhubarb extracts into polyvinyl alcohol/chitosan films yields bio-adsorbent
107 membranes with enhanced structural and functional properties. The optimized formulation,
108 containing 10% Rhubarb extract, exhibited superior antioxidant performance and achieved
109 nearly complete removal ($\approx 96\%$) of both cationic and anionic dyes from wastewater. These
110 findings highlight the potential of plant-derived antioxidants to improve membrane
111 biocompatibility, mechanical stability, and adsorption efficiency for sustainable water treatment
112 applications ²⁵. This adaptability allows researchers to tailor chitosan-based adsorbents to
113 specific applications and optimize their performance for different tasks. For instance, a granular
114 sorbent bead based on chitosan and FeCl₃ was effectively developed to enhance the removal of
115 nitrate and phosphate. The ability to sorb nitrate and phosphate experienced a substantial
116 enhancement. Moreover, the material demonstrated excellent stability and reusability, validated
117 through sorption-desorption cycles ²⁶. Chitosan offers many benefits, such as biodegradability,

118 presence in abundance, biocompatible and non-toxic nature, its limited accessible surface area,
119 low mechanical stability, and partly inaccessible functional groups (due to its semi-crystalline
120 structure), which present challenges for optimal performance ²⁷. To address chitosan's
121 limitations, several modification techniques have been used, employing both physical and
122 chemical methods ²⁸. Compared to pristine chitosan, bead systems derived from this natural
123 polymer exhibit several distinct advantages. For instance, they demonstrate enhanced capacity
124 for removing contaminants from wastewater, offering a promising opportunity for environmental
125 remediation ²⁹.

126 Recent investigations further reinforce the versatility of chitosan-based composites in targeting
127 both cationic and anionic pollutants. For example, Azzeddine *et al.* developed crosslinked and
128 uncrosslinked chitosan gel beads derived from shrimp waste, demonstrating their strong affinity
129 for heavy metal cations and highlighting how bead morphology and crosslinking influence
130 adsorption performance and stability. Under optimized experimental conditions, chitosan gel
131 beads cross-linked with epichlorohydrin achieved a fluoride removal efficiency of 76%, which
132 was notably higher than the 61% removal obtained using non-cross-linked beads ³⁰. Similarly,
133 Alqarni *et al.* reported a crosslinked chitosan–hydroxyapatite–TiO₂ biocomposite that achieved
134 efficient fluoride removal from drinking water, with mechanistic insights confirming the strong
135 binding of oxyanions to the composite framework ³¹. In another study, Alqarni and co-workers
136 synthesized novel chitosan-based surfactants, which showed enhanced interactions with both
137 positively and negatively charged species, thereby extending the applicability of chitosan
138 derivatives for wastewater treatment. A comparative evaluation of Cr(VI) uptake by pristine
139 chitin and the chitin@metakaolin (CHt@M.K.) composite revealed that CHt@M.K. exhibited a
140 markedly higher adsorption capacity of 278.88 mg/g, nearly twice that of chitin, at pH 5.0 within
141 120 minutes. The adsorption behavior was best described by the Langmuir isotherm model,
142 confirming the monolayer nature of Cr(VI) adsorption on CHt@M.K. ³². Furthermore, Algethami
143 *et al.* developed a shrimp waste–derived chitosan-alumina composite that demonstrated efficient
144 removal of hexavalent chromium (Cr(VI)), with an impressive adsorption capacity of 433.12
145 mg/g at pH 4.0 within 120 minutes. The study also highlighted the material's dual advantage of
146 targeting anionic pollutants while maintaining good regeneration potential over successive cycles
147 ³³.

148 Numerous research studies have been undertaken on chitosan to enhance the adsorption
149 properties, and a considerable number of successful outcomes have been achieved so far. For
150 instance, Bernd *et al.* explored the sulfate adsorption capabilities of chitosan bead systems at a
151 pH of 5, utilizing a range of sulfate concentrations between 50 and 1000 mg/L. Their findings
152 revealed that beads with minimal cross-linking demonstrated a moderate sulfate uptake of 35
153 mg/g. On the contrary, beads subjected to cross-linking and subsequent treatment with Ca^{2+}
154 exhibited significantly higher sulfate adsorption, reaching a maximum capacity of 140 mg/g ³⁴.
155 Janek *et al.* investigated the interaction of sulfate ions (SO_4^{2-}) with the polymer chains of
156 chitosan under acidic conditions. The study demonstrated that chitosan serves as an effective
157 adsorbent for sulfate ions, with analysis conducted using an Inductively Coupled Plasma-Optical
158 Emission Spectrometer (ICP-OES) ³⁵. Atif. M *et al.* created a composite material primarily
159 composed of kaolinite(a plentiful mineral in Egypt), a cross-linker copper ion, and chitosan for
160 sulfate and chloride removal from groundwater. In highly acidic conditions, the removal
161 percentages for sulfate and chloride ions reached approximately 92%, while at a neutral pH, the
162 removal rates were around 70% ³⁶. Billah *et al.* (2025) presented a mechanistic study on
163 phosphate (an anionic species) adsorption onto a novel chitosan-based material; their findings
164 reveal insights into adsorption sites, binding mechanisms, and pH dependency, underscoring the
165 capability of chitosan composites for oxyanion removal under realistic conditions. This work
166 adds to the growing evidence that chitosan-based composites can efficiently remove anions such
167 as phosphate in addition to cations ³⁷.

168 However, compared to extensive research on phosphate ³⁸ and nitrate adsorption ³⁹, studies on
169 sulfate adsorption remain insufficient, aligning with recent reviews that highlight limited
170 research on oxyanion (SO_4^{2-}) removal through adsorption, which generates a potential gap to be
171 filled. Thus, this study highlights the significance of employing chitosan-coated iron oxide
172 composite beads and improving adsorption capacity by electrostatic interactions and
173 chemisorption, particularly concerning sustainability. While various adsorbents in the literature
174 show effectiveness but have a low reported adsorption capacity, their limitations become
175 apparent when dealing with trace amounts. There is a demand for increased adsorption
176 performance, especially for lower sulfate concentrations, and with convenient regeneration that
177 offers friendly environmental solutions.

178 In the present study, the iron oxide-incorporated chitosan beads (IOICBs) were synthesized.
179 Briefly, the Fe₃O₄ nanoparticles (NPs) were produced by the co-precipitation method. These NPs
180 were embedded in chitosan using an inverted suspension cross-linking method in the presence of
181 polyvinylpyrrolidone (PVP), which promoted the cross-linking of chitosan. These
182 synthesized IOICBs were then employed to remove sulfate from simulated wastewater via batch
183 adsorption. The effects of pH, initial sulfate concentration, contact time, and dosage on the
184 sulfate removal efficiency of the IOICBs were evaluated. The adsorption isotherms and kinetic
185 models were employed to comprehend the adsorption mechanism and characteristics of the
186 IOICBs, and reusability was tested over four consecutive adsorption cycles.

187 2. MATERIALS AND METHODS

188 2.1 Reagents

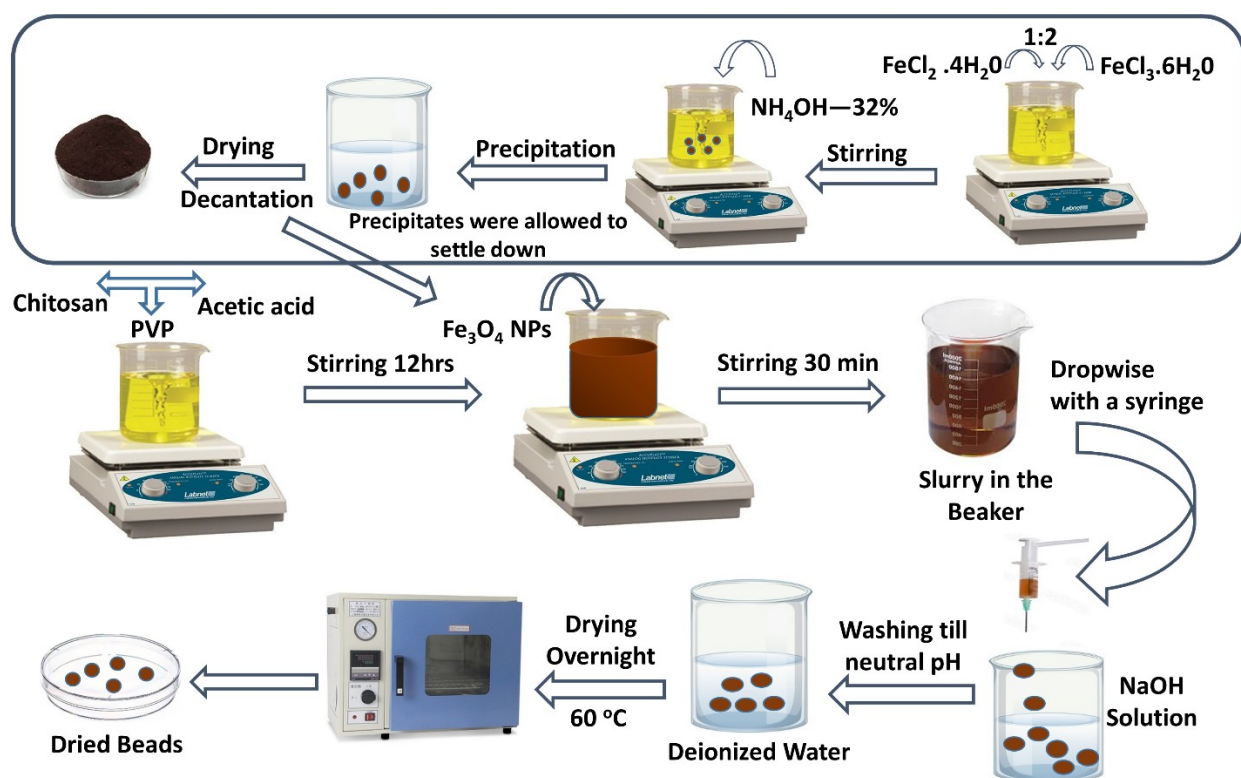
189 A high-viscosity chitosan ((C₆H₁₁NO₄)_n with a molecular mass of 500,000 having 84% level of
190 deacetylation, Sodium sulfate (Na₂SO₄) as a source of sulfate ions, acetic acid (CH₃COOH,
191 glacial 99–100%), hydrochloric acid (HCl), anhydrous sodium hydroxide pellets (NaOH, purity
192 = 98%), and PVP were purchased from Sigma-Aldrich, Germany. For the synthesis of iron
193 oxide, Iron (III) chloride hexahydrate (FeCl₃·6H₂O, M_w = 270.30) and iron (II) chloride
194 tetrahydrate (FeCl₂·4H₂O, M_w = 198.81) were used as received from Duskan, China. Ammonium
195 hydroxide solution (NH₄OH, purity = 32%) was purchased from Merk, South Korea. All
196 analytical grade chemicals obtained were used without any additional purification. MilliQ
197 deionized (DI) water, having low conductivity (< 20 μS/cm), was used throughout this study.

198 2.2 Synthesis of Fe₃O₄ Nanoparticles

199 To prepare iron oxide NPs via the co-precipitation process⁴⁰. Initially, 8 mmol of FeCl₃·6H₂O
200 and 4 mmol of FeCl₂·4H₂O were prepared in DI water (100 mL) using a magnetic stirrer (250
201 rpm) at 20 °C. In this solution, 5 mL of 32% aqueous ammonium hydroxide (NH₄OH) was
202 added to increase the pH of the solution and precipitate the iron oxide (the color turned dark
203 brown from yellow). The supernatant liquid was initially decanted after precipitation, and the
204 residues were washed in DI water multiple times until the pH reached 5.4 at room temperature⁴¹.
205 These precipitates were centrifuged for 2 h at 200 rpm, followed by vacuum filtration and drying
206 overnight at 60 °C in a vacuum oven. The dried residues were ground to fine particles employing
207 pestle and mortar, as shown in Figure 1 (top panel)⁴².

208 **2.3 Synthesis of Iron oxide-incorporated chitosan beads (IOICBs)**

209 IOICBs were prepared using the chemical loading method described before ⁴³. The hybrid beads
210 were created by pouring acetic acid (2.6% v/v) into the solution of chitosan (3.5 g) in 50 mL of
211 polyvinylpyrrolidone (PVP) and agitating at 450 rpm for 12 h. The as-prepared iron oxide NPs (1
212 g) were added to this solution during continuous stirring. This suspension was sonicated for 30
213 min at room temperature for homogenization and deaeration, and then dropwise added to a 1 M
214 NaOH solution to synthesize the IOICBs, which were filtered and washed several times using
215 deionized water. These beads were dried at 60 °C in a vacuum oven for 12 h. A yield of almost
216 4-4.2 g was achieved after some handling/washing losses. The schematic illustration for
217 synthesizing iron oxide NPs and IOICBs is shown in Figure 1.



218

219 **Figure 1.** Schematic representation of the iron oxide NPs (top panel) and the IOICBs synthesis
220 process (bottom panel).

221 **2.4 Characterization**

222 The morphology of the iron oxide NPs and IOICBs was examined using a scanning electron
223 microscope (SEM) (JSM 6700I, JEOL, Japan) at accelerating voltages of 20 kV and 10 kV,
224 respectively. The compositional analysis was performed using an Energy Dispersive

225 Spectroscopy (EDX) detector (JEOL, Japan) attached to this microscope. The formation of Fe₃O₄
226 NPs was confirmed by X-ray (powder) Diffraction (XRD), and the diffraction patterns of the
227 NPs and IOICBs were recorded with a D2 phaser, Bruker Germany, by using Cu-K α radiation (
228 $\lambda=1.54 \text{ \AA}$) and scanning within 20 to 90° of 2 θ angle, having a step size rate of 0.02 s⁻¹. Fourier
229 Transform Infrared spectroscopy (FTIR) of the Fe₃O₄ NPs and IOICBs was performed (both
230 before and after sulfate adsorption) using the Perkin-Elmer-283B FTIR spectrometer (The USA)
231 at 4 cm⁻¹ resolution and within the range of 400 to 4000 cm⁻¹ wavenumber. The Brunauer-
232 Emmett-Teller (BET) method was used to determine the average pore size of the beads and
233 specific surface area measured by N₂ adsorption at 77 K in the ASAP 2420 system
234 (Micromeritics, The USA). The samples were degassed for 1 h at 110 °C before the batch
235 adsorption studies using the VacPrep 061 instrument (Micromeritics, The USA).

236 **2.5 Sulfate removal efficiency and capacity**

237 To perform adsorption studies, the simulated sulfate solutions of various concentrations (30 mL)
238 were initially added to 50 mL laboratory glass bottles. A known amount (adsorbent dosage) of
239 IOICBs was then added to these solutions and stirred by a mechanical shaker for various
240 durations at 120 rpm. Each time, a control solution without IOICBs was placed with an
241 experiment to determine the initial known concentration for comparative calculation. The
242 experiments were performed in triplicate, and mean values are reported. After separating the
243 IOICBs, the remnant solutions were characterized by UV-Vis spectrophotometry (Agilent 8453
244 Spectrophotometer, JENWAY, UK). After adsorption, the sulfate concentration in the test
245 solutions was estimated from the UV-Vis spectra obtained within 200-800 nm wavelengths and
246 compared with the as-prepared sulfate solution. To determine the effect of a single parameter, the
247 conditions of pH (1-8), concentration of sulfate solution (50-300 mg/L), IOICBs dosage (20-50
248 mg), and contact time (6 h) were varied to determine optimum adsorption and mechanism. The
249 adsorption capacity and removal efficiency of the IOICBs for sulfate were calculated using the
250 following formulas (equations 1 and 2, respectively) ^{44,45}.

$$251 \quad q \left(\frac{mg}{g} \right) = \frac{(C_o - C_e)}{m} \times V \quad (1)$$

$$252 \quad \eta = \frac{(C_o - C_e)}{C_o} \quad (2)$$

253 Where C_0 and C_e are the sulfate concentrations in (mg/L) before and after adsorption,
254 respectively. 'V' is the sample volume (L) taken for the analysis, while 'm' is the mass (g) of the
255 adsorbents used during testing.

256 **2.6 Adsorption Isothermal Models**

257 The adsorption mechanism was evaluated by applying the Langmuir and the Freundlich
258 isotherms ⁴⁶. The relative changes in the adsorption and desorption behavior depend on the
259 surface coverage, which was explained by the Langmuir isotherm. Adsorption is proportional to
260 the concentration of the freely available active sites on the surface of the IOICBs (homogenous
261 surface). In contrast, desorption is proportional to the extent of the surface coverage or, in other
262 words, the amount of surface active sites occupied by the adsorbate is dictated by the Langmuir
263 isotherm as given in equation 3 ⁴⁷.

$$264 \frac{C_e}{q_e} = \frac{1}{q_m K_L} + \frac{C_e}{q_m} \quad (3)$$

265 Here, C_e (mg/L) is the concentration of adsorbate at equilibrium, q_e (mg/g) is the amount of
266 adsorbate on the surface of the adsorbent material, whereas q_m (mg/g) is the maximum adsorption
267 capacity of the adsorbent. K_L (mg/g) is the Langmuir constant associated with the variation in the
268 amount of porosity and active surface area of the adsorbent. This suggests that an adsorbent
269 material with a larger surface area and porous structure would increase the adsorption capacity.

$$270 R_L = \frac{1}{1 + K_L C_0} \quad (4)$$

271 Where C_0 (mg/L) is the initial concentration of adsorbate, K_L (mg/g) is the Langmuir constant. R_L
272 provides information about the nature and shape of the adsorption isotherm to be either favorable
273 ($0 < R_L < 1$), unfavorable ($R_L > 1$), linear ($R_L = 1$), or irreversible ($R_L = 0$) as per equation 4.

274 Adsorption on heterogeneous surfaces is subjected to the Freundlich isotherm, which describes
275 the adsorbent surface's heterogeneity, the active sites' distribution, and surface energies as
276 defined in Equation 5 ⁴⁸.

$$277 \log q_e = \log K_F + \frac{1}{n} \log C_e \quad (5)$$

278 Where q_e (mg/g) is the amount of the adsorbed species at equilibrium, C_e (mg/L) is the
279 concentration of adsorbate at equilibrium, K_F (L/mg) is the adsorption capacity, and $1/n$ is the
280 adsorption intensity. These factors indicate that both the relative distribution of energy and the
281 heterogeneity of the adsorbent sites are evaluated from the slope and intercept of the linear plot
282 of $\log q_e$ vs. $\log C_e$, respectively.

283 2.7 Adsorption kinetic models

284 The pseudo-first-order and pseudo-second-order models were tested to investigate the kinetics of
285 sulfate adsorption on the IOICBs^{49,50}. Using equations (6) and (7), the adsorption parameters are
286 calculated as follows:

$$287 \ln(q_e - q_t) = \ln q_e - K_1 t \quad (6)$$

$$288 \frac{t}{q_t} = \frac{1}{K_2 q_e^2} + \frac{t}{q_e}$$

289 (7)

290 Where q_t (mg/g) is the amount of adsorbate adsorbed at a given time 't', q_e (mg/g) is the amount
291 of adsorbate adsorbed at equilibrium, q_t (mg/g) is the amount of adsorbate adsorbed at a time 't',
292 k_1 (1/min) and k_2 (g/(mg.min)) are the rate constant of the pseudo-first and second-order models,
293 respectively⁵¹.

294 2.8 Reusability test

295 A set of experiments was conducted to investigate the regeneration of IOICBs after each
296 adsorption cycle. The regeneration was carried out by first mixing 90 mL of a 250 mg/L sulfate-
297 containing solution (pH = 2) at room temperature for 4 h under continuous stirring. After each
298 adsorption cycle, the IOICBs were washed with DI water three times and treated with 250 mL of
299 1 M NaOH under constant stirring at 120 rpm for 12 h. This allowed the elution of chemically
300 bonded sulfate ions from the IOICBs during desorption. As NaOH was used in low quantities, it
301 posed no environmental hazards. Thus, the IOICBs were washed with plenty of DI water until
302 the pH of the washed water reached the pH of DI water, followed by drying at 60 °C for 4 h and
303 kept in the desiccator until further use.

304 3. RESULTS AND DISCUSSION

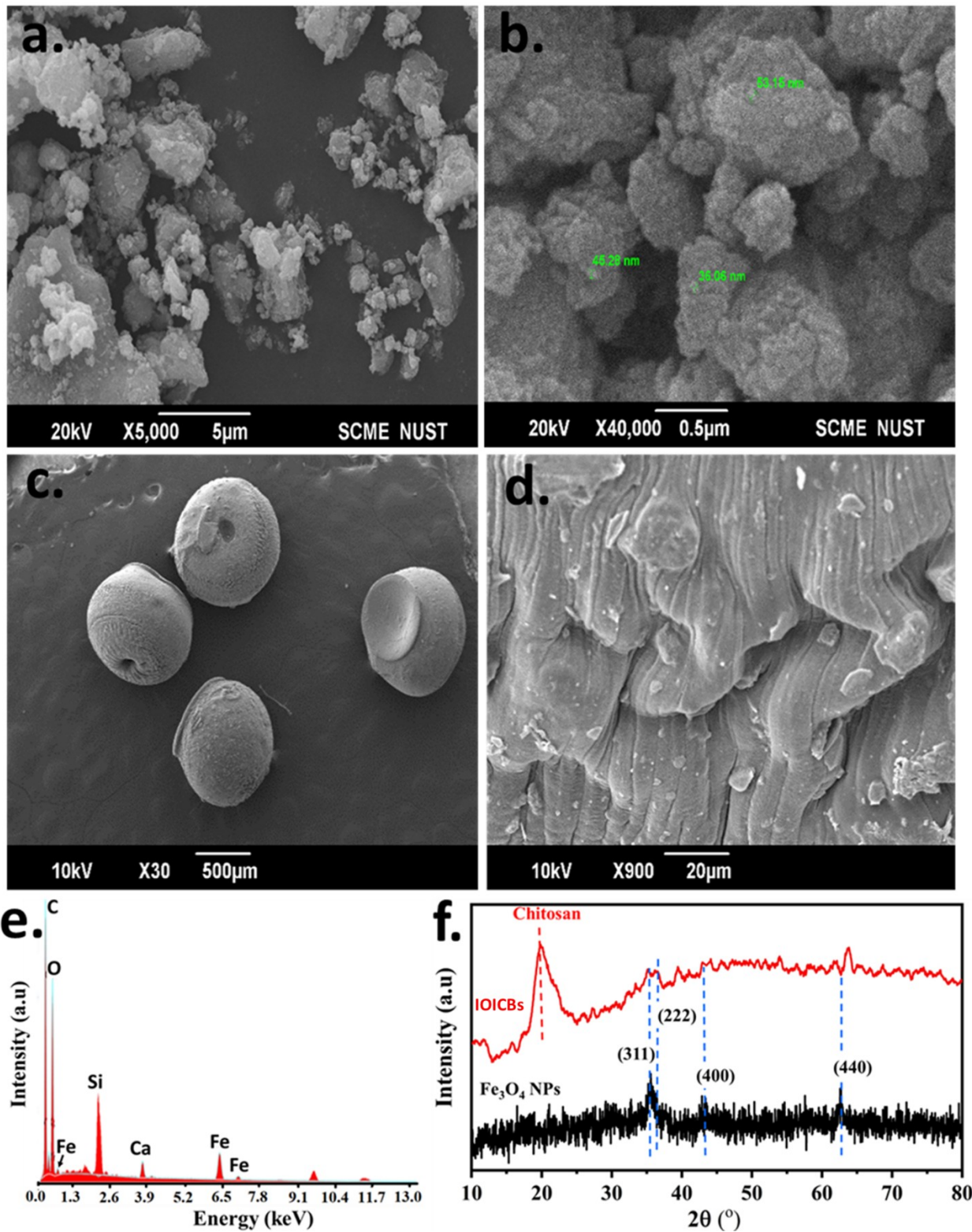
305 3.1 Morphological and Structural Characterization of the IOICBs

306 The morphology of the as-synthesized iron oxide NPs is shown in Figure 2 (a) & (b). The NPs
307 measured from SEM images are found to be of various sizes (36 – 53 nm) and have irregular
308 shapes with porous structures. This is also evident from the BET analysis with a mean NP size =
309 35.7 nm, total area of pores = 68.723 m²/g, total pore volume = 0.03 cm³/g, and specific surface
310 area equaled 167.8606 ± 0.9052 m²/g. In addition, the fine-size iron oxide NPs were found to be
311 agglomerated due to possible steric effects of surface active sites and inter-particulate interaction
312 ^{52,53}. On the other hand, the formation of spherical-shaped (elliptic) micro IOICB is evident in
313 Figure 2(c). The surface morphology of these IOICBs was found to be uneven due to the
314 formation of macro-porous channels within the top chitosan layer. A unidirectional flow pattern
315 was observed on the wall of these macro-pores, which was possibly attributed to the cross-
316 linking groups of chitosan (amine and -OH) in rigorous stirring action of chitosan/PVP/iron
317 oxide NPs, which was facilitated by PVP in the formation of IOICBs, as shown in Figure 2(d).
318 Owing to the formation of the rough and macro-porous surface of the IOICBs, the presence of
319 large amounts of surface active sites can be expected to facilitate sulfate adsorption and be
320 beneficial for better ionic adsorption ⁵⁴. This is confirmed by the BET total area of pores (0.096
321 m²/g) with a total pore volume of 9 × 10⁻⁵ cm³/g and a mean pore width of 1.756 nm.
322 Furthermore, the BET results of IOICBs (0.3255 ± 0.0138 m²/g) firmly agree with the SEM
323 findings. Additionally, the EDX results show that sulfur is absent in the IOICBs sample before
324 sulfate adsorption studies in Figure 2e.

325 The XRD patterns of both iron oxide and IOICBs are shown in Figure 2f. The XRD pattern of
326 the as-synthesized iron oxide NPs suggested the presence of magnetite (Fe₃O₄) as the major
327 phase, following the JCPDS 00-001-1111 reference pattern ⁵⁵. For instance, the diffraction peaks
328 at 2θ of 35.45°, 37.12°, 43.03°, and 62.72° correspond to the diffraction from the (311), (222),
329 (400), and (440) crystallographic planes of magnetite, respectively ⁵⁶. The origin of broader
330 diffraction peaks was attributed to the formation of fine particle size of the Fe₃O₄.

331 The XRD pattern of the IOICBs exhibited the characteristic diffraction peaks of pure chitosan at
332 2θ = 12.17° and 20.16°, which corresponded to crystallinity in the polymeric chains of the
333 chitosan ⁵⁷. These low-intensity broad diffraction peaks were found to be broad and lower in

334 intensity compared to the intensities for pure chitosan. This is due to a loss in the crystallinity of
335 chitosan as it forms an amorphous material with Fe_3O_4 NPs. The magnetic nature of these beads
336 is depicted through the prominent diffraction peaks of magnetite NPs at $2\theta = 35^\circ$ and 62° , more
337 prominently, while other relevant peaks of NPs are also present at $2\theta = 43^\circ$, 53.54° , and 57.16° .
338 The repression of these peaks is seen because of the embedding of magnetite NPs into chitosan
339 beads⁵⁸.



340

341 **Figure 2.** SEM images of Fe₃O₄ NPs (a) low and (b) high magnification, (c) and (d) as-
 342 synthesized IOICBs microbeads, (e) EDX spectrum of IOICBs, and (f) XRD patterns of the
 343 synthesized iron oxide and IOICBs.

344 3.2 Effect of operating parameters

345 The adsorption of sulfate species on IOICBs depends on operating parameters such as solution
346 pH, initial sulfate concentration, IOICBs dose, and overall residence (contact) time of the
347 IOICBs in the sulfate-containing solution. Therefore, to determine the optimized parameters, the
348 maximum adsorption capacity of the as-synthesized IOICBs was determined under various
349 applied conditions, and the results are discussed in the following sections. The experimental data
350 set Table S1, the descriptive statistical analysis (Table S2), the Normal distribution curve of
351 adsorption capacity of sulfate removal (Figure S1), and the Pearson correlation heatmap (Figure
352 S2) demonstrating the interaction behavior between input experimental parameters and
353 adsorption capacity (output) are presented in the supplementary data.

354 3.2.1 Effect of pH

355 The effect of pH on the adsorption capacity of IOICBs was determined in 250 mg/L sulfate
356 solutions. The pH of the solutions was controlled between 1 and 8 with the addition of either HCl
357 or NaOH in the sulfate-containing solutions. To investigate the effect of pH on the effective
358 sulfate removal by IOICBs, the experiments were conducted by adding 50 mg of IOICBs to 30
359 mL of sulfate-containing solutions under vigorous mechanical shaking for 4 h at room
360 temperature (23 ± 1 °C). As depicted in Figure 3 (a), pH significantly influenced the sulfate
361 removal capacity of the IOICBs. Regarding sulfate removal capacity (Q_e), the IOICBs performed
362 better in acidic media than in alkaline conditions. For instance, a maximum sulfate adsorption
363 capacity of 147.6 mg/g was exhibited by the IOICBs at pH 2.0; a similar trend was reported in
364 the literature⁸. The strong electrostatic attraction between the positively charged active sites on
365 the IOICBs and the sulfate anions is believed to be the primary cause of their high adsorption at
366 low pH. The highly acidic environment causes the protonation of the $-NH_2$ functional groups of
367 the chitosan, resulting in the increased electrostatic interaction of the adsorbate anions (i.e.,
368 HSO_4^- and SO_4^{2-})⁵⁹. On the other hand, as stated above, the acidic pH was controlled by adding
369 dilute HCl, and the influence of Cl^- ions on the specific sulfate adsorption was not evaluated.
370 Additionally, the Increased pH of the solution resulted in decreased sulfate ion adsorption due to
371 the poor protonation of the IOICBs. At pH 8, the specific adsorption of OH^- ions could compete
372 with sulfate ions and limit the adsorption capacity of the IOICBs, as evident from the low Q_e
373 value of 142.6 mg/g (Figure 3a). In other words, it is suggested that the partial adsorption of OH^-
374 ions could decrease the sulfate adsorption capacity on the IOICBs surface^{60,61}.

375 3.2.2 Effect of initial sulfate concentration

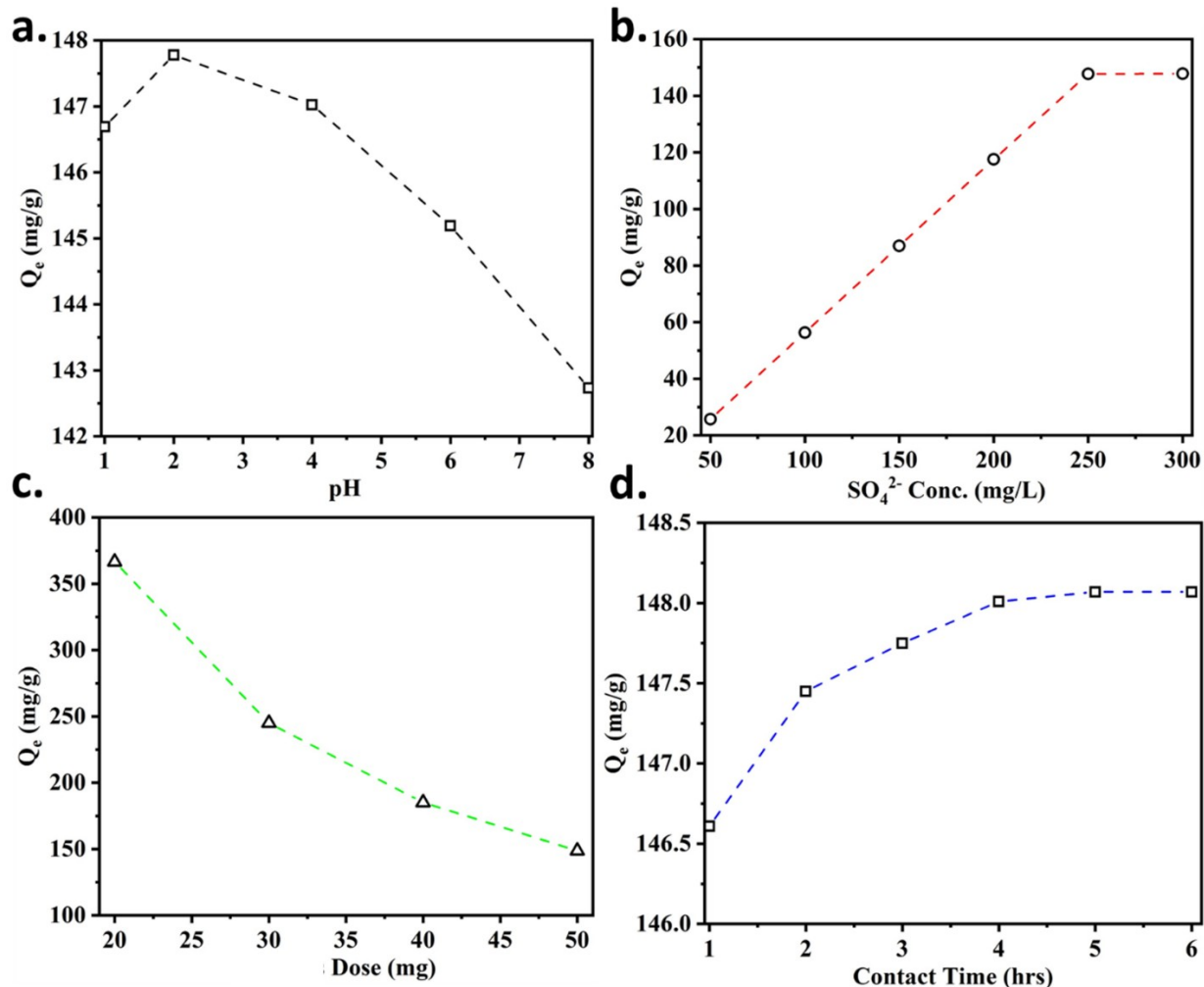
376 To analyze the maximum adsorption capacity of IOICBs as a function of sulfate concentration in
377 water at a pre-optimized pH value of 2 and under the same conditions as prescribed above
378 (section 3.2.1). Figure 3 (b) shows the effect of initial sulfate concentration (varied from 50 to
379 300 mg/L) on the Q_e of the IOICBs at room temperature. A direct relationship between Q_e and
380 initial sulfate concentration was observed from the linear trend up to 250 mg/L initial sulfate
381 concentration. A maximum Q_e of 147 mg/g was measured at this concentration and became
382 constant at sulfate concentration ≥ 250 mg/L, indicating saturation. This highest Q_e demonstrated
383 the maximum sulfate adsorption capacity of the IOICBs. This indicated that after interacting with
384 sulfate ions, the surface active sites within the porous structure of IOICBs become fully saturated
385 with sulfate species and represent the maximum surface coverage achievable under applied
386 conditions. It is essential to mention that the maximum adsorption of the sulfate ions is possible
387 if these species can readily approach the surface pores of the IOICBs; thus, rigorous mechanical
388 shaking applied during this process is considered helpful. In addition to mechanical shaking, the
389 increase in initial concentration of the sulfate ions could also facilitate the effective mass
390 transport of the sulfate species towards the active sites on the IOICBs, which could also avoid
391 the development of a concentration gradient at the IOICBs/solution interface ^{61,62}.

392 3.2.3 Effect of IOICB dose

393 The amount of IOICBs used in the adsorption analysis is critical in defining the effluent
394 concentration and significantly influences the process economics. Various IOICB dosages (from
395 20 – 50 mg) were tested in 30 mL of solution containing 250 mg/L of sulfate concentration,
396 having a pH of 2.0 and a residence time of 4 h, under continuous stirring conditions at room
397 temperature. A decline in Q_e was observed with an increase in IOICB concentration, attributed to
398 the saturation of the surface active sites and the limiting amount of sulfate ions left in the
399 solution with an excess of IOICB dosage. Notably, the amount of sulfate adsorbed (in mg) by the
400 IOICBs can be calculated by multiplying Q_e by the dosage in grams. The maximum adsorption
401 was achieved at 0.02 g of IOICB dosage, as elucidated in Figure 3c. These results indicated that
402 compared to the 0.05 g of IOICBs dosage, the amount of sulfate removed from the solution was
403 slightly higher at 0.02 and 0.03 g of IOICBs dosage. Based on these results, approximately 1.67
404 g of IOICBs per liter (equal to 50 mg in 30 mL in this study) of the solution was considered the
405 optimal concentration to achieve maximum sulfate adsorption for further tests ^{61,63}.

406 3.2.4 *Effect of contact time*

407 The effect of IOICB contact time with the sulfate-containing solution is also an important
408 parameter to optimize process conditions. Figure 3d shows the slight increase in Q_e with contact
409 time, and it becomes constant beyond 4 h. In other words, the adsorption efficiency of the
410 IOICBs achieved its saturation limit during 4 h of interaction with the sulfate solution and
411 remained independent of the contact duration. These results indicated that under applied acidic
412 conditions, the initial adsorption of sulfate ions on the IOICBs was found to be fast, which
413 gradually slowed down owing to the increase in surface coverage and decreased availability of
414 the free active sites for further sulfate adsorption. In other words, it is believed that specific
415 adsorption of sulfate ions on IOICBs proceeds in two phases: rapid initial adsorption of the
416 sulfate ions in the first 2 h, followed by a time-dependent adsorption to reach the maximum
417 (saturation limit) after 4 h ⁶⁴.



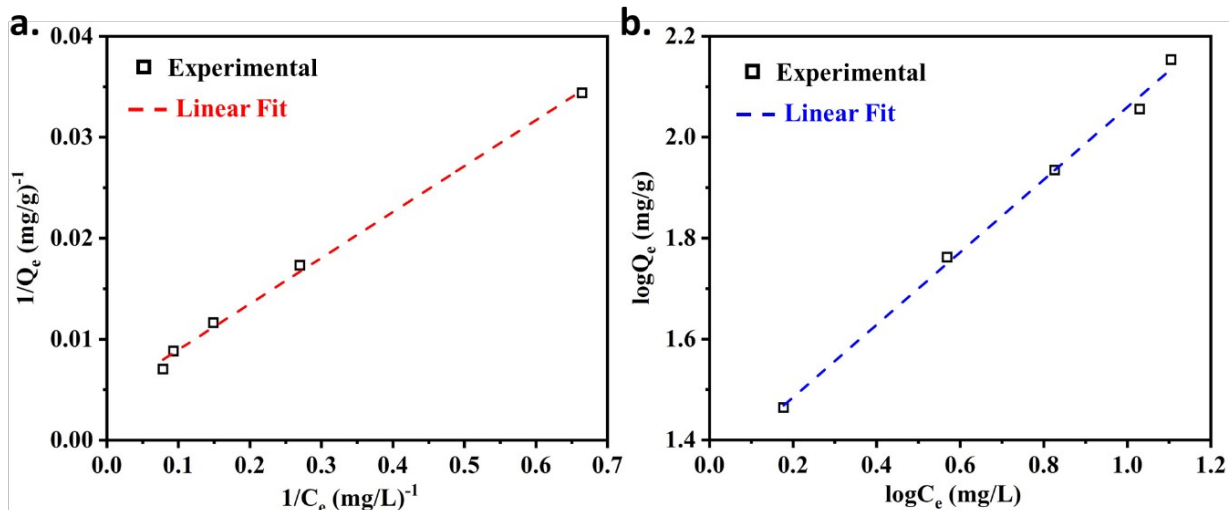
418

419 **Figure 3.** Effect of (a) pH, (b) initial sulfate concentration, (c) IOICBs dose, and (d) IOICBs
 420 contact time on the adsorption capacity of IOICBs for sulfate species at room temperature.

421 3.3 Adsorption Isotherms

422 The adsorption isotherms were obtained under the optimized conditions described above, i.e., 50
 423 mg or (1.67 g/L) IOICBs dosage was added in sulfate-containing solutions having a pH of 2
 424 under continuous stirring on a mechanical shaker for 4 h at room temperature (23 °C). As per
 425 Langmuir and Freundlich's isotherms, the adsorption capacity was plotted vs. equilibrium sulfate
 426 concentration, as shown in Figure 4. A comparison between these isotherms and the
 427 experimental data was made, and the validity of these models was assessed based on linear
 428 fitting (R^2 values), as given in Table 1. The Langmuir isotherm exhibits monolayer adsorption of
 429 the sulfate, suggesting homogeneously organized identical active sites on the surface of the
 430 adsorbent material. On the other hand, the Freundlich model is governed by the adsorption of

431 species in multilayers and represents the interaction between the adsorbed molecules in addition
 432 to surface coverage at the active site. In other words, the Freundlich isotherm also implies that
 433 adsorption is independent of the number of available active sites on the adsorbent surface.



434
 435 **Figure 4.** Representation of the adsorption isotherms model fitting (a) Langmuir and (b) the
 436 Freundlich isotherms.

437

438

439

440 **Table 1.** The obtained parameters for sulfate adsorption on IOICBs at room temperature (23 °C)
 441 after Langmuir and the Freundlich isotherm model fitting.

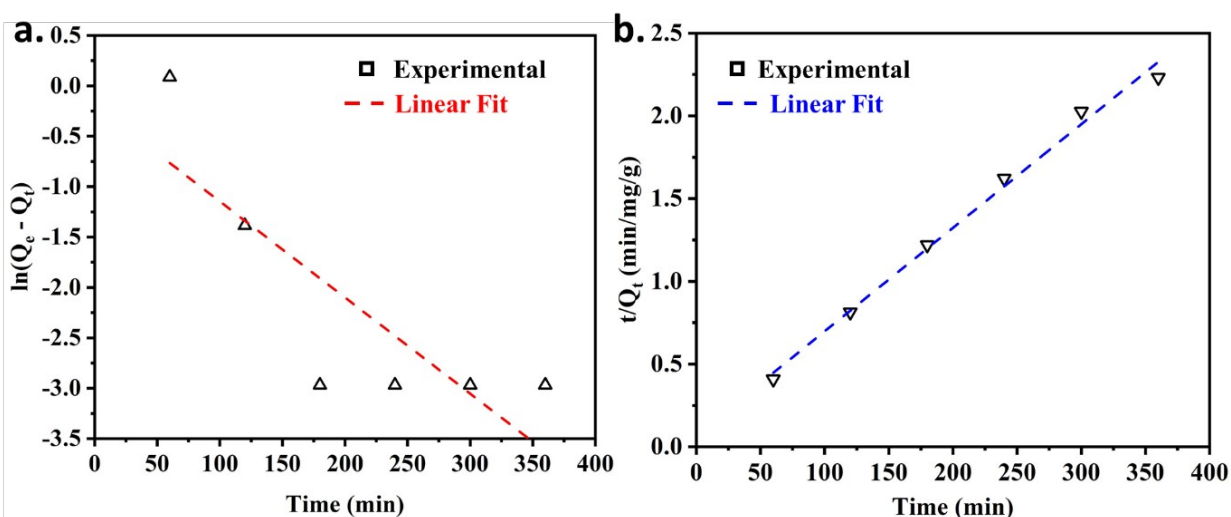
| Langmuir Model | | | | | Freundlich Model | | | | |
|----------------------|-----------------|-------|--------|--------|------------------|-----------------|--------|--------|--------|
| Q_{\max} (mg/g) | K_L (mg/g) | R^2 | AIC | BIC | N | K_F (L/mg) | R^2 | AIC | BIC |
| 226.75 | 498.87 | 0.997 | -56.59 | -57.37 | 1.391 | 3.822 | 0.9960 | -23.57 | -24.35 |

442

443 3.4 Adsorption kinetics

444 Figure 5 shows a comparison between experimental data with the pseudo-first (equation 6) and
 445 pseudo-second-order (equation 7) kinetic models for the adsorption process. The experimental
 446 data had a good linear fit to the pseudo-second-order adsorption model ($R^2 = 0.992$). In contrast,

447 the regression coefficient ($R^2 = 0.694$) is a total misfit with the experimental data for the pseudo-
 448 first-order kinetic model. The equilibrium adsorption capacity from experimental data (148.07
 449 mg/g) is close to the predicted value of 159.74 mg/g using pseudo-second order, compared to the
 450 value of 0.823 mg/g obtained from pseudo-first-order, as shown in Table 2. Also, the 2nd order
 451 adsorption rate constant of 2.2×10^{-3} (g/(mg.min)) is suitable and justified by the interaction
 452 mechanism. Therefore, based on these results, it is suggested that the chemisorption process
 453 mainly governs sulfate adsorption on IOICBs.



454
 455 **Figure 5.** Kinetics of sulfate adsorption on IOICBs as predicted from the (a) Pseudo 1st order and
 456 (b) Pseudo 2nd order kinetic models.

457 **Table 2.** Sulfate adsorption–kinetic parameters obtained from fitting experimental data with the
 458 pseudo 1st- and 2nd-order kinetic models.

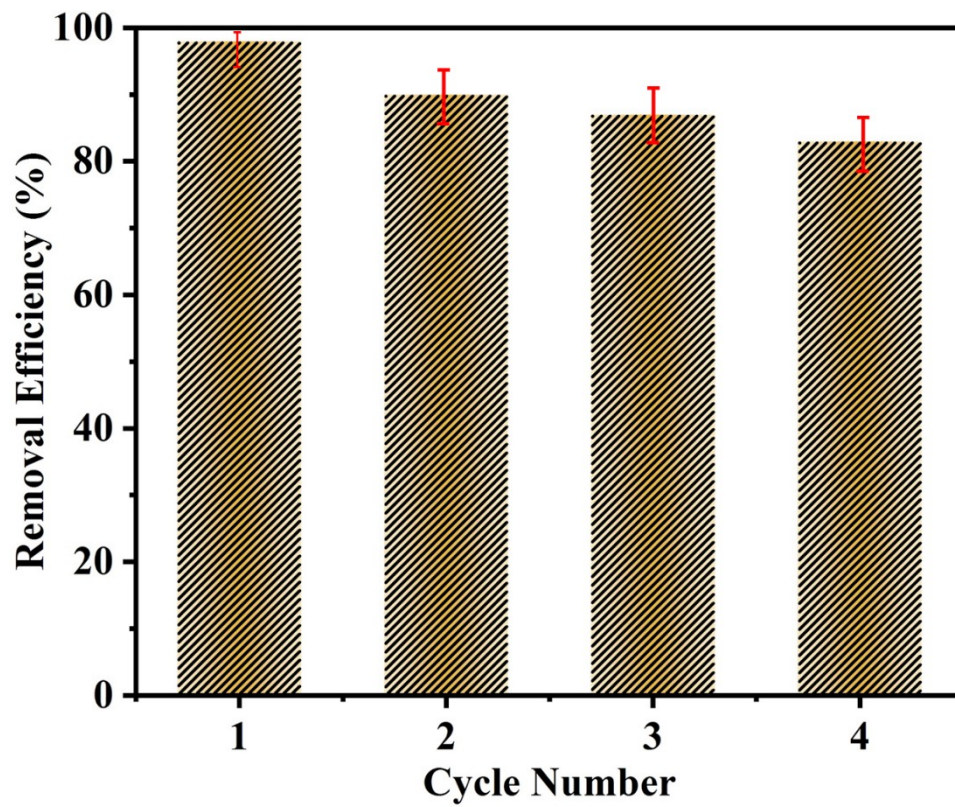
| Pseudo 1 st order | | | | | Pseudo 2 nd order | | | | |
|------------------------------|------------------------|-------|-------|-------|------------------------------|-----------------------|-------|--------|--------|
| Q_e (mg/g) | K_1 (1/min) | R^2 | AIC | BIC | Q_e (mg/g) | K_2 (g/(mg.min)) | R^2 | AIC | BIC |
| 0.823 | -2.64×10^{-5} | 0.694 | 15.83 | 15.42 | 159.74 | 2.22×10^{-3} | 0.992 | -13.55 | -13.96 |

459

460 3.5 Regeneration Studies and Mechanism

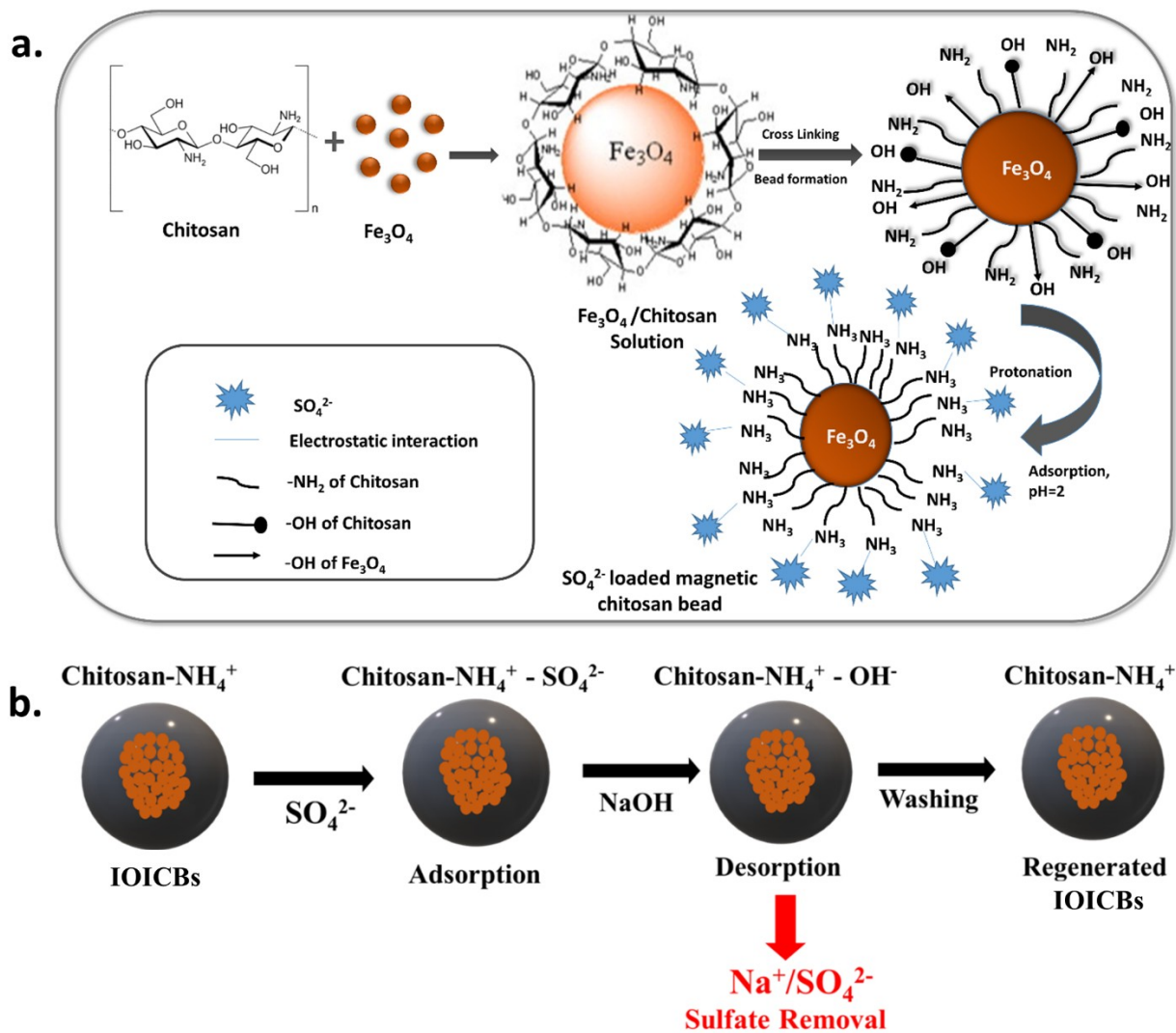
461 The IOICBs were repeatedly used with fresh solution for four adsorption/regeneration cycles to
 462 evaluate their cyclic stability and adsorption capacity. As shown in Figure 6, the adsorption
 463 efficiency of the IOICBs gradually decreased over four repetitive adsorption/regeneration cycles.

464 For instance, 98% adsorption efficiency was obtained for fresh IOICBs, which declined to
465 approximately 83% after 4 cycles. These results highlighted that during repetitive adsorption and
466 regeneration cycles, the degradation of the surface functionality compromised the adsorption
467 capacity and sulfate removal efficiency of the IOICBs. This behavior could be explained by
468 understanding the adsorption mechanism, as shown in Figure 7. Briefly, during the adsorption
469 process, the presence of acidic NH_4^+ functional groups on the surface of chitosan facilitates the
470 chemisorption of the sulfate ions. These adsorbed sulfate ions can be removed from the surface
471 by treating the IOICBs in NaOH solution. Owing to the competing adsorption of the OH and
472 removal of SO_4^{2-} , regeneration of the IOICBs was possible. Under acidic conditions, the
473 protonation of the surface functional groups would increase the concentration of NH_4^+ species,
474 resulting in the regeneration of the IOICBs for reuse. However, it is suggested that during the
475 regeneration process, the OH^- species remained partially adsorbed on the active sites and reduced
476 the adsorption capacity of IOICBs for SO_4^{2-} species⁶⁵. Thus, the process of sulfate adsorption on
477 IOICBs was highly pH-dependent. A study of magnetic chitosan-Fe (III) hydrogels was reported
478 to have a positive charge below pH 7⁶⁶. Another study reported the zero-point charge of Fe_3O_4 -
479 chitosan beads to be 6.94, which indicates that at pH below this value, the adsorbent remains
480 positively charged for enhanced adsorption removal, while at pH >6.94, this adsorbent becomes
481 negatively charged⁴³. In acidic media, the protonation of the $-\text{NH}_2$ species significantly
482 improved the electrostatic interaction of SO_4^{2-} species. Instead, an increase in pH led to the
483 preferential adsorption of $-\text{OH}$ species on the IOICB's surface in comparison to the sulfate
484 species. Furthermore, the partial amount of SO_4^{2-} species could irreversibly adsorb on the surface
485 of IOICBs, decreasing their loading capacity, as discussed below.



486

487 **Figure 6.** Effect of cyclic adsorption/regeneration of IOICBs on the sulfate removal efficiency.



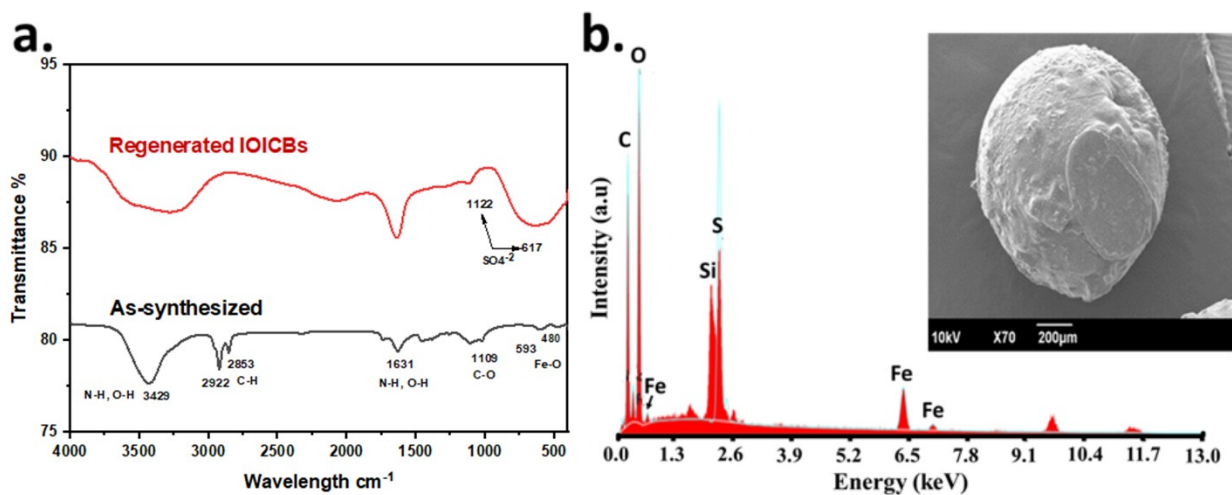
488

489 **Figure 7.** (a) Removal mechanism (top squared panel) and (b) Regeneration for sulfate
 490 adsorption/desorption (bottom panel) on IOICBs.

491 3.6 Post characterization of IOICBs after cyclic regeneration

492 In comparison, the structural characterization of the as-synthesized and regenerated IOICBs was
 493 also done using FTIR spectroscopy. As shown in Figure 8a, the presence of C–H, NH₂, and –OH
 494 functional groups was evident. For instance, the absorption bands observed at 3427 cm⁻¹ and
 495 1633 cm⁻¹ were linked to the vibrations of –OH and –NH bands⁶⁷. The peaks originating at 480
 496 cm⁻¹ and 593 cm⁻¹ are attributed to the Fe–O bond vibrations, highlighting the presence of Fe₃O₄
 497 in the IOICBs. The stretching vibrations of C–O bonds were observed at 1109 cm⁻¹. On the
 498 surface of as-synthesized IOICBs, the bands observed at 2922 cm⁻¹ and 2853 cm⁻¹ correspond to
 499 the vibrational stretching of the C–H bonds in methyl (–CH₃) and alkyl (–CH₂) groups,

500 respectively ⁶⁸. In the case of regenerated IOICBs, the appearance of a broad peak at 3429 cm⁻¹
501 and a more intense peak at 1631 cm⁻¹ validates the presence of –OH, –NH stretching vibrations
502 ⁶⁹. On the other hand, the peaks at 1122 and 617 cm⁻¹ are associated with the vibrations of S–O
503 and S-O-S bonds in the sulfate species that remained chemisorbed on the surface of IOICBs
504 during the adsorption/regeneration process ⁷⁰⁻⁷². The presence of sulfur species on the surface of
505 IOICBs was confirmed through EDX analysis, indicating specific adsorption of SO₄²⁻ as depicted
506 in Figure 8b compared to no intensity of sulfur in pristine IOICBs (Figure 2e). The presence of
507 these species on the regenerated IOICBs could be associated with the irreversible sulfate
508 adsorption of SO₄²⁻, which resulted in a decrease in adsorption capacity, as evident in the
509 successive regeneration cycles (Figure 6). The physical appearance of the IOICBs remained
510 unchanged after the adsorption process, demonstrating their structural integrity and stability
511 throughout the adsorption/regeneration process. In terms of loss in adsorption capacity, no
512 significant physical change in the morphology was observed. Based on this behavior, the
513 decrease in adsorption capacity is likely due to the permanent occupation of SO₄²⁻ species on the
514 active sites during the cyclic adsorption/regeneration process. Based on the information
515 provided, the developed IOICBs show superior performance compared to other adsorbents,
516 namely cross-linked chitosan beads and activated carbon, in terms of sulfate removal.
517 Specifically, at low doses, the as-synthesized IOICBs have the highest adsorption capacity
518 (147.7 mg/g) under highly acidic conditions, as shown in Table 3. The high performance is
519 indicated by the porous structural morphology on the surface of chitosan beads, which is evident
520 from SEM results. This suggests that the IOICBs could be a more effective and efficient choice
521 for sulfate removal under these specific conditions. However, further information is needed to
522 fully evaluate the comparative performance of the different adsorbents, including factors such as
523 cost, ease of synthesis, and other relevant parameters.



524

525 **Figure 8.** Characterization of the IOICBs after cyclic adsorption/regeneration process (a) FTIR
 526 spectra, (b) EDX analysis, and morphology of the retrieved IOICB.

527

528 **Table 3.** Comparing the sulfate adsorption capacity of IOICBs with other adsorbent materials
 529 reported in the literature.

| Adsorbent | Adsorption capacity (mg/g) | pH | Concentration C ₀ (ppm) | Reference(s) |
|---|----------------------------|----------|------------------------------------|-------------------|
| IOICBs | 147.7 | 2 | 250 | This study |
| Hardwood-based AC modified with polypyrrole | 45 | 7-7.2 | 250 | 73 |
| Cross-linked chitosan beads | 35 | 5 | 1000 | 8,34 |
| Cross-linked Chitosan beads | 140 | 5 | 1000 | 34 |
| Modified Rice straw | 75 | 6.4 | 500 | 8 |
| Poly(m-phenylenediamine) | 109 | <3 | 500 | 74 |

530

531 4. CONCLUSION

532 Iron oxide (Fe_3O_4) NPs were produced using the co-precipitation method and were used to
533 synthesize surface-functionalized chitosan beads (IOICBs) successfully. Based on SEM, XRD,
534 and FTIR analyses, the cross-linking $-\text{OH}$ and $-\text{NH}_2$ groups of the chitosan shell with cubical-
535 shaped porous Fe_3O_4 NPs in the core were found to be an effective adsorbent for the removal of
536 sulfate from mine water. The total pore volume and surface area of IOICBs were further
537 supported by BET analysis. The effects of various parameters (i.e., pH of the solution, initial
538 sulfate ions concentration, IOICBs dose, and contact time) on the adsorption behavior of IOICBs
539 were studied in batch mode. Effective sulfate removal (147.7 mg/g) was obtained at pH 2, a
540 sulfate concentration of 250 mg/L, and room temperature (23 °C) with a contact time of 4 h. The
541 experimental adsorption data conformed to the Langmuir model ($R^2 = 0.997$), whereas the
542 adsorption kinetics perfectly agreed with the pseudo-second-order model ($R^2 = 0.992$). The
543 synthesized IOICBs were successfully reused in 4 cycles and regenerated with an overall ~17%
544 decay in adsorption capacity. Overall, under acidic conditions, the synthesized IOICBs presented
545 good adsorption capacity and effective sulfate removal efficiency during four successive
546 loading/regeneration cycles, owing to the protonation of the $-\text{NH}_2$ species, which significantly
547 improved the electrostatic interaction of SO_4^{2-} species. Furthermore, the easy magnetic separation
548 of the IOICBs from solution and their fast kinetics make them a promising material for sulfate
549 removal from mine water.

550 ACKNOWLEDGMENTS

551 The authors express their gratitude to the National University of Sciences and Technology
552 (NUST) Research Directorate and the Higher Education Commission (HEC) of Pakistan for
553 providing the necessary technical assistance and financial support per NRPU Project No. 6020.
554 The author (M.Y) gratefully acknowledge the support from the European Just Transition Fund
555 within the Operational Programme: Just Transition under the aegis of the Ministry of the
556 Environment of the Czech Republic, project CirkArena number
557 CZ.10.03.01/00/22_003/0000045 and the Ministry of Education Youth and Sports of the Czech
558 Republic, Operational Programme Johannes Amos Comenius OP JAC "Application potential
559 development in the field of polymer materials in the context of circular economy compliance
560 (POCEK)", number CZ.02.01.01/00/23_021/0009004. The authors are further grateful for co-

561 funding from the development process of the Centre of Polymer Systems, Tomas Bata University
562 in Zlin, program DKRVO (RP/CPS/2024-28/002) supported by the Ministry of Education Youth
563 and Sports of the Czech Republic. M.Y also expresses his gratitude for support within the
564 “Creativity, Intelligence & Talent for the Zlin Region” (CIT - ZK) program.

565 **DATA AVAILABILITY STATEMENT**

566 The study includes all the data that support the findings and conclusions, which can be found
567 within the article and supplementary data file.

568 **CONFLICT OF INTEREST**

569 The authors declare there exists no form of competing interests.

570 **Credit authorship contribution statement**

571 **Uswa Zahra:** Experimental Work, Methodology, Investigation, Data analyses, Writing- original
572 draft.

573 **Imran Ahmad Khan:** Methodology, Formal analysis, experimental design and support.

574 **Asad Ullah Khan:** Formal analysis, experimental design and support.

575 **Muhammad Yasir:** Data curation, Funding acquisition, Writing- Review & editing.

576 **Wenjuan Zhang:** Conceptualization, Writing- Review & editing.

577 **Kashif Mairaj Deen:** Data Analysis, critical review, and editing.

578 **Edouard Asselin:** Critical review and editing.

579 **Rehan Sadiq:** Investigation, Conceptualization, Formal analysis.

580 **Muhammad Nouman Aslam Khan:** Software, Data curation.

581 **Nasir M. Ahmad:** Conceptualization, Supervision, Project administration, Funding acquisition,
582 Review & editing.

583 **REFERENCES**

584 1. Fernando WAM, Ilankoon IMSK, Syed TH, Yellishetty M. Challenges and opportunities
585 in the removal of sulphate ions in contaminated mine water: A review. *Miner Eng.*

- 586 2018;117:74-90. doi:<https://doi.org/10.1016/j.mineng.2017.12.004>
- 587 2. LIAO G li, LIAO D xue, LI Q ming. Heavy metals contamination characteristics in soil of
588 different mining activity zones. *Trans Nonferrous Met Soc China*. 2008;18(1):207-211.
589 doi:[https://doi.org/10.1016/S1003-6326\(08\)60037-0](https://doi.org/10.1016/S1003-6326(08)60037-0)
- 590 3. Wantzen KM, Mol JH. Soil Erosion from Agriculture and Mining: A Threat to Tropical
591 Stream Ecosystems. *Agriculture*. 2013;3(4):660-683. doi:10.3390/agriculture3040660
- 592 4. Chen G, Ye Y, Yao N, Hu N, Zhang J, Huang Y. A critical review of prevention,
593 treatment, reuse, and resource recovery from acid mine drainage. *J Clean Prod*.
594 2021;329:129666. doi:<https://doi.org/10.1016/j.jclepro.2021.129666>
- 595 5. Bowell R. A review of sulfate removal options for mine waters. *Proc Mine Water 2004-*
596 *Process, Policy Prog*. Published online January 1, 2004.
- 597 6. Barr A. Sulphate removal by nanofiltration. *Filtr Sep*. 2001;38(6):18-20.
598 doi:[https://doi.org/10.1016/S0015-1882\(01\)80376-1](https://doi.org/10.1016/S0015-1882(01)80376-1)
- 599 7. Öztürk Y, Ekmekçi Z. Removal of sulfate ions from process water by ion exchange resins.
600 *Miner Eng*. 2020;159:106613. doi:<https://doi.org/10.1016/j.mineng.2020.106613>
- 601 8. Cao W, Dang Z, Zhou XQ, et al. Removal of sulphate from aqueous solution using
602 modified rice straw: Preparation, characterization and adsorption performance. *Carbohydr*
603 *Polym*. 2011;85(3):571-577. doi:<https://doi.org/10.1016/j.carbpol.2011.03.016>
- 604 9. Kinnunen P, Kyllönen H, Kaartinen T, Mäkinen J, Heikkinen J, Miettinen V. Sulphate
605 removal from mine water with chemical, biological and membrane technologies. *Water*
606 *Sci Technol*. 2018;2017:wst2018102. doi:10.2166/wst.2018.102
- 607 10. Dąbrowski A. Adsorption — from theory to practice. *Adv Colloid Interface Sci*.
608 2001;93(1):135-224. doi:[https://doi.org/10.1016/S0001-8686\(00\)00082-8](https://doi.org/10.1016/S0001-8686(00)00082-8)
- 609 11. HUANG G, YANG C, ZHANG K, SHI J. Adsorptive Removal of Copper Ions from
610 Aqueous Solution Using Cross-linked Magnetic Chitosan Beads. *Chinese J Chem Eng*.
611 2009;17(6):960-966. doi:[https://doi.org/10.1016/S1004-9541\(08\)60303-1](https://doi.org/10.1016/S1004-9541(08)60303-1)
- 612 12. Quesada HB, de Araújo TP, Vareschini DT, de Barros MASD, Gomes RG, Bergamasco

- 613 R. Chitosan, alginate and other macromolecules as activated carbon immobilizing agents:
614 A review on composite adsorbents for the removal of water contaminants. *Int J Biol*
615 *Macromol.* 2020;164:2535-2549. doi:<https://doi.org/10.1016/j.ijbiomac.2020.08.118>
- 616 13. Chagas PMB, Caetano AA, Rossi MA, et al. Chitosan-iron oxide hybrid composite:
617 mechanism of hexavalent chromium removal by central composite design and theoretical
618 calculations. *Environ Sci Pollut Res.* 2019;26(16):15973-15988. doi:10.1007/s11356-019-
619 04545-z
- 620 14. Li M, Kang Y, Ma H, Dong J, Wang Y, Kuang S. Efficient removal of heavy metals from
621 aqueous solutions using Mn-doped FeOOH: Performance and mechanisms. *Environ Res.*
622 2023;231:116161. doi:<https://doi.org/10.1016/j.envres.2023.116161>
- 623 15. Upadhyay U, Sreedhar I, Singh SA, Patel CM, Anitha KL. Recent advances in heavy
624 metal removal by chitosan based adsorbents. *Carbohydr Polym.* 2021;251:117000.
625 doi:<https://doi.org/10.1016/j.carbpol.2020.117000>
- 626 16. Vieira RS, Meneghetti E, Baroni P, et al. Chromium removal on chitosan-based sorbents –
627 An EXAFS/XANES investigation of mechanism. *Mater Chem Phys.* 2014;146(3):412-
628 417. doi:<https://doi.org/10.1016/j.matchemphys.2014.03.046>
- 629 17. Medina RP, Nadres ET, Ballesteros FC, Rodrigues DF. Incorporation of graphene oxide
630 into a chitosan–poly(acrylic acid) porous polymer nanocomposite for enhanced lead
631 adsorption. *Environ Sci Nano.* 2016;3(3):638-646. doi:10.1039/C6EN00021E
- 632 18. Zhang Y, Lin S, Qiao J, et al. Malic acid-enhanced chitosan hydrogel beads (mCHBs) for
633 the removal of Cr(VI) and Cu(II) from aqueous solution. *Chem Eng J.* 2018;353:225-236.
634 doi:<https://doi.org/10.1016/j.cej.2018.06.143>
- 635 19. Shariful MI, Sharif S Bin, Lee JLL, Habiba U, Ang BC, Amalina MA. Adsorption of
636 divalent heavy metal ion by mesoporous-high surface area chitosan/poly (ethylene oxide)
637 nanofibrous membrane. *Carbohydr Polym.* 2017;157:57-64.
638 doi:<https://doi.org/10.1016/j.carbpol.2016.09.063>
- 639 20. Ngamsurach P, Namwongsa N, Praipipat P. Synthesis of powdered and beaded chitosan
640 materials modified with ZnO for removing lead (II) ions. *Sci Rep.* 2022;12.

- 641 doi:10.1038/s41598-022-22182-4
- 642 21. Abulyazied DE, Isawi H, Ali ES, et al. Fabrication and characterization of magnetic cobalt
643 ferrite intercalated chitosan grafted polyaniline ternary nanocomposites for removing
644 some heavy metals simultaneously. *J Mol Liq.* 2024;393:123527.
645 doi:<https://doi.org/10.1016/j.molliq.2023.123527>
- 646 22. Moustafa H, Ahmed EM, Hemida M, Rabee M, Isawi H. Surface grafting GO
647 nanoplatelets with antimicrobial rosin acids for strengthening photocatalytic of
648 chitosan/gelatin nanocomposites. *Diam Relat Mater.* 2025;157:112552.
649 doi:<https://doi.org/10.1016/j.diamond.2025.112552>
- 650 23. Ahmed EM, Isawi H, Morsy M, Hemida MH, Moustafa H. Effective nanomembranes
651 from chitosan/PVA blend decorated graphene oxide with gum rosin and silver
652 nanoparticles for removal of heavy metals and microbes from water resources. *Surfaces
653 and Interfaces.* 2023;39:102980. doi:<https://doi.org/10.1016/j.surfin.2023.102980>
- 654 24. Moustafa H, Shemis MA, Ahmed EM, Isawi H. Improvement of hybrid polyvinyl
655 chloride/dapsone membrane using synthesized silver nanoparticles for the efficient
656 removal of heavy metals, microorganisms, and phosphate and nitrate compounds from
657 polluted water. *RSC Adv.* 2024;14(28):19680-19700. doi:10.1039/D4RA03810J
- 658 25. Isawi H, Ahmed EM, Rabee M, Moustafa H. Using natural antioxidant Rhubarb extracts
659 in PVA/chitosan bio-adsorbent films for efficient removal of cationic and anionic dyes
660 from polluted water. *J Ind Eng Chem.* 2025;141:626-644.
661 doi:<https://doi.org/10.1016/j.jiec.2024.09.049>
- 662 26. Cui X, Li H, Yao Z, et al. Removal of nitrate and phosphate by chitosan composited beads
663 derived from crude oil refinery waste: Sorption and cost-benefit analysis. *J Clean Prod.*
664 2019;207:846-856. doi:<https://doi.org/10.1016/j.jclepro.2018.10.027>
- 665 27. Pillai CKS, Paul W, Sharma CP. Chitin and chitosan polymers: Chemistry, solubility and
666 fiber formation. *Prog Polym Sci.* 2009;34(7):641-678.
667 doi:<https://doi.org/10.1016/j.progpolymsci.2009.04.001>
- 668 28. Marpu SB, Benton EN. Shining Light on Chitosan: A Review on the Usage of Chitosan

- 669 for Photonics and Nanomaterials Research. *Int J Mol Sci.* 2018;19(6).
670 doi:10.3390/ijms19061795
- 671 29. Wang J. Removal of various pollutants from water and wastewater by modified chitosan
672 adsorbents. *Crit Rev Environ Sci Technol.* 2018;47:1-56.
673 doi:10.1080/10643389.2017.1421845
- 674 30. Azzeddine T, Marrane SE, Goudali O, et al. Simple and modified chitosan gel beads from
675 a natural source as a bio-sorbent for water defluoridation: Experimental and computational
676 perspectives. *Inorg Chem Commun.* 2024;167:112752.
677 doi:<https://doi.org/10.1016/j.inoche.2024.112752>
- 678 31. Alqarni LS, Algethami JS, EL Kaim Billah R, et al. Synthesis and characterization of a
679 crosslinked deacetylated chitin modified chicken bone waste-derived hydroxyapatite and
680 TiO₂ biocomposite for defluoridation of drinking water. *Int J Biol Macromol.*
681 2024;282:136839. doi:<https://doi.org/10.1016/j.ijbiomac.2024.136839>
- 682 32. Algethami JS, Jugade R, Billah El Kaim R, et al. Chitin extraction from crab shells and
683 synthesis of chitin @metakaolin composite for efficient amputation of Cr (VI) ions.
684 *Environ Res.* 2024;252:119065. doi:<https://doi.org/10.1016/j.envres.2024.119065>
- 685 33. Algethami JS, Billah REK, Alhamami MAM, et al. Confiscation of Cr(VI) by cross-linked
686 shrimp waste-derived chitosan @Al₂O₃ nanocomposite: Experimental and theoretical
687 approach. *J Mol Struct.* 2025;1321:140182.
688 doi:<https://doi.org/10.1016/j.molstruc.2024.140182>
- 689 34. Steiger BGK, Wilson LD. Modular Chitosan-Based Adsorbents for Tunable Uptake of
690 Sulfate from Water. *Int J Mol Sci.* 2020;21(19). doi:10.3390/ijms21197130
- 691 35. Weißpflog J, Boldt R, Kohn B, et al. Investigation of mechanisms for simultaneous
692 adsorption of iron and sulfate ions onto chitosan with formation of orthorhombic
693 structures. *Colloids Surfaces A Physicochem Eng Asp.* 2020;592:124575.
694 doi:<https://doi.org/10.1016/j.colsurfa.2020.124575>
- 695 36. Mohamed AMG, Mubarak MF, Snousy MG, et al. Using modified clay-chitosan
696 composite filter as a second stage in the conventional iron and manganese removal plant

- 697 system to eliminate permanent hardness anions in drinkable groundwater. *Environ Adv.*
698 2023;13:100407. doi:<https://doi.org/10.1016/j.envadv.2023.100407>
- 699 37. EL Kaim Billah R, Khan MA, Essenni S, et al. A mechanistic insight into anionic
700 phosphate adsorption on developed chitosan.ZnO@metakaolin biocomposite. *Int J Biol*
701 *Macromol.* 2025;308:142405. doi:<https://doi.org/10.1016/j.ijbiomac.2025.142405>
- 702 38. Manna A, Naskar N, Sen K, Banerjee K. A review on adsorption mediated phosphate
703 removal and recovery by biomatrices. *J Indian Chem Soc.* 2022;99(10):100682.
704 doi:<https://doi.org/10.1016/j.jics.2022.100682>
- 705 39. Liu Y, Zhang X, Wang J. A critical review of various adsorbents for selective removal of
706 nitrate from water: Structure, performance and mechanism. *Chemosphere.*
707 2022;291:132728. doi:<https://doi.org/10.1016/j.chemosphere.2021.132728>
- 708 40. Zeng Q, Baker I, Loudis J, Liao Y, Hoopes PJ. Synthesis and heating effect of iron/iron
709 oxide composite and iron oxide nanoparticles - art. no. 64400H. *Proc Soc Photo Opt*
710 *Instrum Eng.* 2007;6440:13. doi:10.1117/12.708182
- 711 41. Pawar S, Takke A. Regulatory Aspects, Types and Bioapplications of Metallic
712 Nanoparticles: A Review. *Curr Drug Deliv.* 2023;20(7):857-883.
713 doi:10.2174/1567201819666220817110025
- 714 42. Saqib S, Farooq M, Munis H, et al. Synthesis, characterization and use of iron oxide nano
715 particles for antibacterial activity. *Microsc Res Tech.* Published online June 23, 2020.
- 716 43. Karthikeyan P, Meenakshi S. Fabrication of hybrid chitosan encapsulated magnetic-kaolin
717 beads for adsorption of phosphate and nitrate ions from aqueous solutions. *Int J Biol*
718 *Macromol.* 2021;168:750-759. doi:<https://doi.org/10.1016/j.ijbiomac.2020.11.132>
- 719 44. Ding L, Guo C, Zhu Y, et al. Adsorptive removal of gallic acid from aqueous solution
720 onto magnetic ion exchange resin. *Water Sci Technol.* 2020;81. doi:10.2166/wst.2020.236
- 721 45. Lambert N, Van Aken P, Van den Broeck R, Dewil R. Adsorption of phosphate on iron-
722 coated sand granules as a robust end-of-pipe purification strategy in the horticulture
723 sector. *Chemosphere.* 2021;267:129276.
724 doi:<https://doi.org/10.1016/j.chemosphere.2020.129276>

- 725 46. Zhan Y, Lin J, Zhu Z. Removal of nitrate from aqueous solution using cetylpyridinium
726 bromide (CPB) modified zeolite as adsorbent. *J Hazard Mater.* 2011;186(2):1972-1978.
727 doi:<https://doi.org/10.1016/j.jhazmat.2010.12.090>
- 728 47. Jothinathan L, Sozhan G, Vasudevan S. Recovery of hydrogen and removal of nitrate
729 from water by electrocoagulation process. *Environ Sci Pollut Res Int.* 2012;20.
730 doi:[10.1007/s11356-012-1028-4](https://doi.org/10.1007/s11356-012-1028-4)
- 731 48. Banu HAT, Karthikeyan P, Vigneshwaran S, Meenakshi S. Adsorptive performance of
732 lanthanum encapsulated biopolymer chitosan-kaolin clay hybrid composite for the
733 recovery of nitrate and phosphate from water. *Int J Biol Macromol.* 2020;154:188-197.
734 doi:<https://doi.org/10.1016/j.ijbiomac.2020.03.074>
- 735 49. Qiu H, Lv L, Pan C, Zhang Q jian, Zhang W ming, Zhang Q xing. Critical review in
736 adsorption kinetic models. *J Zhejiang Univ Sci A.* 2009;10:716-724.
737 doi:[10.1631/jzus.A0820524](https://doi.org/10.1631/jzus.A0820524)
- 738 50. Wang J, Guo X. Adsorption kinetic models: Physical meanings, applications, and solving
739 methods. *J Hazard Mater.* 2020;390:122156.
740 doi:<https://doi.org/10.1016/j.jhazmat.2020.122156>
- 741 51. Hu Q, Chen N, Feng C, Zhang J, Hu W, Lv L. Kinetic studies of nitrate removal from
742 aqueous solution using granular chitosan-Fe(III) complex. *Water Sci Technol.*
743 2015;73(5):1211-1220. doi:[10.2166/wst.2015.596](https://doi.org/10.2166/wst.2015.596)
- 744 52. Takai Z, Mustafa M, Asman S, Sekak K. Preparation and Characterization of Magnetite
745 (Fe₃O₄) nanoparticles By Sol-Gel Method. *Int J Nanoelectron Mater.* 2019;12:37-46.
- 746 53. Hussain A, Jadhav A, Baek YK, Choi H, Lee J, Kang Y. One Pot Synthesis of Exchange
747 Coupled Nd₂Fe₁₄B/alpha-Fe by Pechini Type Sol-Gel Method. *J Nanosci Nanotechnol.*
748 2013;13:7717-7722. doi:[10.1166/jnn.2013.7833](https://doi.org/10.1166/jnn.2013.7833)
- 749 54. Gambhir RP, Parthasarathy AK, Sharma S, Kale S, Magdum VV, Tiwari AP. pH-
750 responsive glycine functionalized magnetic iron oxide nanoparticles for SARS-CoV-2
751 RNA extraction from clinical sample. *J Mater Sci.* 2022;57(28):13620-13631.
752 doi:[10.1007/s10853-022-07464-6](https://doi.org/10.1007/s10853-022-07464-6)

- 753 55. Xu J, Yang H, Fu W, et al. Preparation and magnetic properties of magnetite nanoparticles
754 by sol-gel method. *J Magn Magn Mater*. 2007;309(2):307-311.
755 doi:<https://doi.org/10.1016/j.jmmm.2006.07.037>
- 756 56. Zheng Y hui, Cheng Y, Bao F, Wang Y sheng. Synthesis and magnetic properties of
757 Fe₃O₄ nanoparticles. *Mater Res Bull*. 2006;41(3):525-529.
758 doi:<https://doi.org/10.1016/j.materresbull.2005.09.015>
- 759 57. Durán S V, Lapo B, Meneses M, Sastre AM. Recovery of Neodymium (III) from Aqueous
760 Phase by Chitosan-Manganese-Ferrite Magnetic Beads. *Nanomaterials*. 2020;10(6).
761 doi:10.3390/nano10061204
- 762 58. Rorrer GL, Hsien TY, Way JD. Synthesis of porous-magnetic chitosan beads for removal
763 of cadmium ions from wastewater. *Ind Eng Chem Res*. 1993;32(9):2170-2178.
764 doi:10.1021/ie00021a042
- 765 59. Nassar NN. Rapid removal and recovery of Pb(II) from wastewater by magnetic
766 nanoadsorbents. *J Hazard Mater*. 2010;184(1):538-546.
767 doi:<https://doi.org/10.1016/j.jhazmat.2010.08.069>
- 768 60. Cengeloglu Y, Tor A, Ersoz M, Arslan G. Removal of nitrate from aqueous solution by
769 using red mud. *Sep Purif Technol*. 2006;51(3):374-378.
770 doi:<https://doi.org/10.1016/j.seppur.2006.02.020>
- 771 61. Mohammadi E, Daraei H, Ghanbari R, et al. Synthesis of carboxylated chitosan modified
772 with ferromagnetic nanoparticles for adsorptive removal of fluoride, nitrate, and
773 phosphate anions from aqueous solutions. *J Mol Liq*. 2019;273:116-124.
774 doi:<https://doi.org/10.1016/j.molliq.2018.10.019>
- 775 62. Ao H, Cao W, Hong Y, Wu J, Wei L. Adsorption of sulfate ion from water by zirconium
776 oxide-modified biochar derived from pomelo peel. *Sci Total Environ*. 2020;708:135092.
777 doi:<https://doi.org/10.1016/j.scitotenv.2019.135092>
- 778 63. Chen Y, Wang J. Removal of radionuclide Sr²⁺ ions from aqueous solution using
779 synthesized magnetic chitosan beads. *Nucl Eng Des*. 2012;242:445-451.
780 doi:<https://doi.org/10.1016/j.nucengdes.2011.10.059>

- 781 64. Dong T. Nitrogen removal from groundwater using scoria: Kinetics, equilibria and
782 microstructure. *J Environ Sci Health A Tox Hazard Subst Environ Eng*. 2021;56:1-8.
783 doi:10.1080/10934529.2021.1883958
- 784 65. Chang CF, Chang CY, Hsu TL. Removal of fluoride from aqueous solution with the
785 superparamagnetic zirconia material. *Desalination*. 2011;279(1):375-382.
786 doi:https://doi.org/10.1016/j.desal.2011.06.039
- 787 66. Yu Z, Zhang X, Huang Y. Magnetic Chitosan–Iron(III) Hydrogel as a Fast and Reusable
788 Adsorbent for Chromium(VI) Removal. *Ind Eng Chem Res*. 2013;52(34):11956-11966.
789 doi:10.1021/ie400781n
- 790 67. Eltaweil AS, Ibrahim K, Abd El-Monaem EM, El-Subruiti GM, Omer AM. Phosphate
791 removal by Lanthanum-doped aminated graphene oxide@aminated chitosan
792 microspheres: Insights into the adsorption mechanism. *J Clean Prod*. 2023;385:135640.
793 doi:https://doi.org/10.1016/j.jclepro.2022.135640
- 794 68. Tran HV, Tran LD, Nguyen TN. Preparation of chitosan/magnetite composite beads and
795 their application for removal of Pb(II) and Ni(II) from aqueous solution. *Mater Sci Eng C*.
796 2010;30(2):304-310. doi:https://doi.org/10.1016/j.msec.2009.11.008
- 797 69. El-Monaem E, Salah Ayoup M, Omer A, Hammad E, Eltaweil A. Sandwich-like
798 construction of a new aminated chitosan Schiff base for efficient removal of Congo red.
799 *Appl Water Sci*. 2023;13. doi:10.1007/s13201-023-01866-w
- 800 70. Kiefer J, Stärk A, Kiefer A, Glade H. Infrared Spectroscopic Analysis of the Inorganic
801 Deposits from Water in Domestic and Technical Heat Exchangers. *Energies*. 2018;11:798.
802 doi:10.3390/en11040798
- 803 71. Vidya YS, Lakshminarasappa BN. Preparation, Characterization, and Luminescence
804 Properties of Orthorhombic Sodium Sulphate. Pavesi L, ed. *Phys Res Int*.
805 2013;2013:641631. doi:10.1155/2013/641631
- 806 72. Periasamy A, Muruganand S, Palaniswamy M. Vibrational studies of Na₂SO₄, K₂SO₄,
807 NaHSO₄ and KHSO₄ crystals. *Rasayan J Chem*. 2009;2:981-989.
- 808 73. Hong S, Cannon FS, Hou P, Byrne T, Nieto-Delgado C. Adsorptive removal of sulfate

809 from acid mine drainage by polypyrrole modified activated carbons: Effects of
810 polypyrrole deposition protocols and activated carbon source. *Chemosphere*.
811 2017;184:429-437. doi:<https://doi.org/10.1016/j.chemosphere.2017.06.019>

812 74. Pizarro C, Escudey M, Bravo C, Gacitua M, Pavez L. Sulfate Kinetics and Adsorption
813 Studies on a Zeolite/Polyammonium Cation Composite for Environmental Remediation.
814 *Minerals*. 2021;11:180. doi:10.3390/min11020180

815